Assessment of turbulence modeling for engineering prediction of swirling vortices in the near burner zone

R. Weber and B. M. Visser
International Flame Research Foundation, The Netherlands

F. Boysan
Flow Simulation Ltd., Sheffield, UK

Measurements and computations of a number of isothermal swirling flows are reported. The focus is on two categories of swirling flows: high confinement flows in geometries representative of gas turbines and low confinement flows encountered in industrial and experimental furnaces. The flow geometries consisted of a solid-body vortex generator, a burner quarl, and a cylindrical furnace.

The measurement techniques utilized are discussed, with emphasis on measurement errors. In order to identify the flow features that the computer models are expected to predict, the physics of the flows is treated in detail.

In the finite difference computations, three models of turbulence were tested: a Reynolds stress model (RSM), an algebraic stress model (ASM), and the k–ε model. Attention was paid to numerical related errors, and an effort was made to minimize the effect of numerical diffusion. A major conclusion is that reliable predictions of swirling vortices that were originally in solid-body rotation can be made, if fine numerical grids are used in conjunction with the QUICK method and either the RSM or the ASM. In terms of the overall flow structure, no substantial differences between the RSM and ASM predictions were observed. In the solid-body-rotation flows analyzed, the transport of the Reynolds stresses was of little importance.

Keywords: fluid dynamics; swirling confined flows; turbulence modeling

Introduction

Swirling flows are frequently encountered in many types of combustion equipment. Combustion engineers designing an aircraft gas combustor, a ramjet combustor, or a pulverized coal burner utilize properties of the internal recirculation zone (IRZ), which is formed in the vicinity of the burner when high swirl is imposed on the flow. The IRZ properties determine not only the flame's shape, stability, and heat release rates, but also emissions of nitrogen oxides. Recognition of these effects led to intensive research during recent decades.[1–5]

Recent IFRF research on methods of NOx reduction with pulverized coal firing was focused on internal air staging and application of fuel-rich precombustors.[6,7] In the internal air-staging techniques, a fuel-rich zone is generated in the vicinity of the burner by separating a substantial portion of the secondary air stream from the primary particle-laden flow. This can be accomplished by a swirl burner design that generates the appropriate fluid-flow pattern in the near burner zone.[6,7]

In parallel with the burner development experiments, the task of developing a mathematical model that can predict properties of the near burner zone of swirl stabilized, pulverized coal flames was undertaken. A computer code possibly can greatly assist understanding the near burner field. In the future, the code can perhaps serve as a design and burner development tool.

Address reprint requests to Dr. Weber at the International Flame Research Foundation, P.O. Box 10.000, 1970 CA IJmuiden, The Netherlands.

Received 13 October 1988; accepted 16 January 1990

Objectives

Computation of swirling flows is difficult. Large velocity gradients appear in these flows, so numerical problems and turbulence modeling play an important role in their analysis. We decided therefore to assess several models of turbulence for computing swirling flows. In this article we focus on two categories of flows: high confinement flows in geometries representative of gas turbines and low confinement flows encountered in industrial and experimental furnaces.

In the 1980s, a marked shift from the k–ε turbulence model toward second-order turbulence modeling took place.[8] These second-order turbulence closures can be classified generally as Reynolds stress models (RSM), in which all the stresses are calculated from their transport equations, and algebraic stress models (ASM). In the latter models, stress transport is represented algebraically in terms of the transport of turbulence energy. Providing a review of all the work on the application of turbulence models to swirling-flow predictions is beyond the scope of this article. However, two recent publications are relevant in the context of this study. The work of Fu *et al.*[9] deals with the strongly swirling free jet measured by Sislian and Cusworth[10] and the weakly swirling jet measured by Ribeiro and Whitelaw.[11] The free jets were computed with both an ASM and a RSM. Fu *et al.* carried out the computations

on a 40×35 grid using a second-order quadratic upstream-weighted differencing method for convective transport. They concluded that the ASM "ought not to be used in axisymmetric swirling flows where stress-transport processes give rise to significant terms in the overall Reynolds-stress budget." Our article deals with confined swirling flows, where most of the stress is generated on the boundary of the reverse-flow region. We demonstrate later that, for such swirling flows, ASM predictions are in close agreement with RSM results.

Hogg and Leschziner[12] carried out computations of a highly swirling confined flow measured by So *et al.*[13] The computations were performed on 48×48 grid with both an RSM and the k–ε model. They introduced some corrections to the pressure–strain term into their RSM in the vicinity of the walls. These corrections accounted for redistribution of fluctuating velocities in the direction normal to the wall. They concluded that properties of subcritical downstream flow could be properly predicted only when the RSM is applied. We demonstrate later that the ASM used in our study can predict downstream subcritical flow almost as well as the RSM can.

The overall assessment of turbulence modeling is carried out here from an engineering point of view. First, we expect that the mathematical modeling correctly predicts overall flow pattern and time mean velocities. Second, we expect reasonable predictions of turbulent kinetic energy levels. By computing a number of swirling flows with the three models of turbulence applied, we attempt to identify turbulence closures for engineering computations of such flows.

We discuss the measurement techniques applied, emphasizing measurement errors, prior to assessing the turbulence model. In order to identify flow features that the computer models are to predict, we provide a detailed discussion of the physics of the flows.

The measurements

The IFRF project on near field aerodynamics (NFA) of swirling flows provides systematic experimental data on expanding swirling flows. Both axial and tangential components of the mean velocity vector, together with their normal stresses, were measured for many combinations of both quarl and furnace geometries, which are shown in Figure 1.

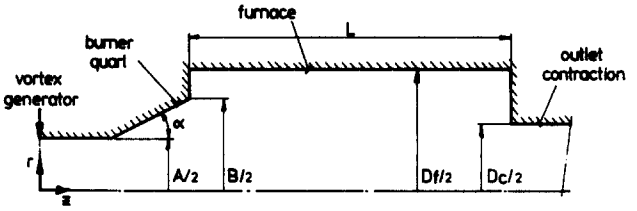

Figure 1 Furnace geometry, with the arrow at $z=0$ indicating the end of the vortex generator

Table 1 lists the four solid-body-rotation flows considered in this study. For consistency, the cases are numbered as in References 14 and 15. In all cases the swirl was generated by a rotating honeycomb, so the initial vortices had a solid-body rotation. The swirl generator and the geometry of the experimental rig were designed in such a way that the swirling flows had negligible (zero) radial velocity downstream from the generator. The Reynolds number for all flow cases was about 50,000. The level of turbulence of the generated flows—measured just upstream of the burner quarl—also is listed in Table 1. The level of inlet turbulence is defined as:

$$i = \frac{\overline{u^2} + \overline{v^2} + \overline{w^2}}{2U_0^2} \tag{1}$$

Table 1 Considered solid-body-rotation flows ($A = 190$ mm; C = conical quarl)

	High confinement			Low confinement
NFA case no.	3	11	40	9
Swirl number [−]	0.7	0.7	0.7	0.7
Turb. level [%]	1	1	5	1
Quarl type	C	C	C	C
B/A [−]	1.5	2	2	1.5
α	20°	20°	20°	20°
D_f [mm]	290	440	440	960
D_c [mm]	290	440	440	440

Notation

A	Throat diameter
B	Diameter of burner quarl outlet
C	Circulation
C_0	Circulation of the inlet vortex
C_1, C_2	Coefficients in pressure strain model
$C_{\varepsilon 1}$, $C_{\varepsilon 2}$, C_μ	Constants of the turbulence models
D_{ij}	Net diffusion rate of stress component $\overline{u_i u_j}$
D_f	Diameter of the furnace
D_c	Diameter of furnace end contraction
$E(u_i)$	Integrated fluxes of turbulence
E_t	Flow energy
H	Bernouli function
W_{max}	Maximum value of tangential velocity for initial solid-body rotation vortices
P	Production rate of turbulence energy
P_{ij}	Production rate of stress component $\overline{u_i u_j}$
S_0	Swirl number at the vortex generator
t	Time
U_0	Mass mean axial velocity
U_p	Mass mean velocity of the central jet
U_a	Mass mean velocity of the annular flow
U, V, W	Mean velocities in the axial, radial, and circumferential directions
u, v, w	Fluctuating velocities in the axial, radial, and circumferential directions
U_i, u_i	Mean and fluctuating velocities (tensor notation) in direction x_i
i	Inlet turbulence level
$\overline{uv}$, $\overline{vw}$, $\overline{uw}$	Components of the Reynolds stress
$\overline{v^2}$, $\overline{u^2}$, $\overline{w^2}$	tensor ($\overline{u_i u_j}$)
r	Cylindrical coordinate
z	Axial distance from the vortex generator

Greek symbols

α	Quarl half-angle
δ_{ij}	Kronecker delta
ε	Kinematic dissipation rate of turbulent energy
	fluid density
σ_k, σ_ε	Constants of the turbulence model
Ψ	Stream function
Ψ_{ij}	Pressure strain correlation of stress component $\overline{u_i u_j}$

The initial swirl number shown in Table 1 was calculated from the measured axial and tangential velocities:

$$S_0=\frac{\int_0^{A/2} WUr^2\,dr}{\frac{A}{2}\int_0^{A/2} U^2 r\,dr} \tag{2}$$

which for solid-body-rotation vortices can be simplified further to:

$$S_0=\frac{W_{\max}}{2U_0} \tag{3}$$

The quality of the measurement data

Velocity information was obtained with a laser-Doppler velocimeter employing a 3-W argon-ion laser operated at a wave length of 514.5 nm. Sensitivity of the equipment to flow direction was provided by frequency shifting. A 600-mm front lens was applied along with a beam translator, allowing variance of beam separation. The result was a transfer function, which in the absence of frequency shift, was 0.246, 0.164, or 0.0821 MHz m s^{-1}. The output from the photomultiplier was mixed with a signal derived from the driving frequency of the Bragg cell, and the resulting signal was processed by a filter-bank processor of the UK Harwell Laboratory. The flows were seeded with magnesium oxide particles of diameter smaller than 1 μm.

Statistically reliable mean and turbulent velocities require a sufficiently large number of data events. Hence usually 2,000 data-event measurements were taken at each point. When 20,000 data points were sampled, the measured mean velocities deviated only $\pm 3.0\%$ from those obtained from 2,000 data points. For fluctuating (normal) components, a deviation of $\pm 4\%$ was observed.

For any LDA technique, the data acquisition rate depends on flow velocity. Usually, more data are acquired for high velocities than for low velocities, and therefore we believe that the measured mean velocities may be biassed toward high values. Although one did not correct for velocity biasing, we believe that the effect is small. The reason is that the absolute values of measured velocities were in the range of 0–8 m s^{-1}.

In order to examine the repeatability of the experimental results, the LDA measurements of cases 3 and 11 were repeated four weeks later. The values of both mean axial and tangential velocities differed by only a small percentage, whereas the maximum differences in fluctuating velocities were on the order of 10%.

The strength of an IRZ is defined as the maximum reverse flow in the IRZ, normalized by the inlet flow. The values of both reverse flow and inlet flow are obtained by integrating the measured values of axial velocities. We estimated that, for small ($D_f=290$ mm) and medium-sized furnaces ($D_f=440$ mm), the integration of measured negative axial velocities results in an error of $\pm 10\%$. For large furnaces ($D_f=960$ mm), 15–20% is applicable.

Computing isothermal swirling vortices

The computation of turbulent flows requires that the continuity equation,

$$\frac{\partial}{\partial x_i}(\rho U_i)=0 \tag{4}$$

and the momentum conservation equation,

$$\frac{\partial}{\partial x_i}\rho U_i U_j=-\frac{\partial p}{\partial x_j}+\frac{\partial}{\partial x_i}\mu\left(\frac{\partial U_i}{\partial x_j}+\frac{\partial U_j}{\partial x_i}\right)-\frac{\partial}{\partial x_i}\rho\overline{u_i u_j} \tag{5}$$

be accompanied by a model of turbulence that relates the Reynolds stresses $\overline{u_i u_j}$ to known or calculable quantities.

Turbulence modeling

Three turbulence models were considered in this study: RSM, ASM, and k–ε.

The Reynolds stress model (RSM). The Reynolds stress transport equation,

$$\frac{D\overline{u_i u_j}}{Dt}=P_{ij}+\Psi_{ij}-\tfrac{2}{3}\varepsilon\delta_{ij}+D_{ij} \tag{6}$$

can provide an anisotropic turbulence closure. The diffusion term and the pressure–strain correlation are calculated as follows:[16,17]

$$D_{ij}=\frac{\partial}{\partial x_k}\mu_t\frac{\partial\overline{u_i u_j}}{\partial x_k} \tag{7}$$

$$\Psi_{ij}=-C_1\frac{\varepsilon}{k}(\overline{u_i u_j}-\tfrac{2}{3}k\delta_{ij})-C_2(P_{ij}-\tfrac{2}{3}P\delta_{ij}) \tag{8}$$

where $P=\frac{1}{2}P_{ii}$ and P_{ij} is given by

$$P_{ij}=-\overline{u_i u_k}\frac{\partial U_i}{\partial x_k}-\overline{u_i u_k}\frac{\partial U_j}{\partial x_k} \tag{9}$$

The RSM, as applied here for axisymmetric swirling flow configurations, consists of five transport equations for the following stresses or their combinations: $\overline{uv}$, $\overline{vw}$, $\overline{uw}$, $\overline{v^2}-\overline{u^2}$, and $\overline{v^2}-\overline{w^2}$. These five equations are accompanied by transport equations for kinetic energy, k, and its dissipation rate, ε. We first computed the Reynolds stresses from their transport equations and then coupled them into the momentum equations. The model constants were prescribed values, as proposed in the original literature on the modeling of individual terms of Equation 6: $C_\mu=0.09$, $C_{\varepsilon 1}=1.44$, $C_{\varepsilon 2}=1.92$, $\sigma_k=1.0$, $\sigma_\varepsilon=1.3$, $C_1=2.5$, and $C_2=0.55$.[18,19]

The algebraic stress model (ASM). The partial differential transport equations, Equations 6 can be reduced to algebraic form using Rodi's approximation:[20]

$$\frac{D\overline{u_i u_j}}{Dt}-D_{ij}=\frac{(P-\varepsilon)\overline{u_i u_j}}{k} \tag{10}$$

Equation 10 is exact when the ratio $\overline{u_i u_j}/k$ is constant throughout the flow field.

Although Rodi's algebraic approximation may not be completely valid, there is a strong temptation to apply it, because it transforms the partial differential transport equations into algebraic equations. Potentially, there is a lot to gain—in terms of simplicity—but the resulting algebraic equations are difficult to solve and couple with the momentum equations of swirling flows, in particular. Therefore in the literature, there are many variations of algebraic stress models. In some of the models only the most important stresses are calculated from the algebraic equations and incorporated into the momentum equations. Often the stresses are incorporated into the momentum equations by a modification to the constant C_μ.[21]

We coupled the Reynolds stresses into the momentum equations by adding and subtracting diffusion terms that involve the k–ε eddy-viscosity model to the momentum equations,

Equation 5:

$$\frac{\partial}{\partial x_i}\rho U_i U_j = -\frac{\partial p}{\partial x_j}+\frac{\partial}{\partial x_i}(\mu+\mu_t)\left(\frac{\partial U_i}{\partial x_j}+\frac{\partial U_j}{\partial x_i}\right) -\left[\frac{\partial}{\partial x_i}\rho\overline{u_i u_j}+\frac{\partial}{\partial x_i}\mu_t\left(\frac{\partial U_i}{\partial x_j}+\frac{\partial U_j}{\partial x_i}\right)\right] \tag{11}$$

In this way, the term in brackets in Equation 11 can be interpreted as a perturbation to the k–ε model and is treated in the computer program as a source term. This approach yields very stable results and is far superior to the previously used technique of modifying the C_μ constant.

Another important aspect of algebraic stress modeling relates to the appearance of so-called added convection, when Equation 10 is transformed to cylindrical polar coordinates and when swirl is present. The algebraic equations that relate individual Reynolds stresses to the rate of strain are

$$\overline{u_i u_j}=\tfrac{2}{3}k\delta_{ij}+\frac{1-C_2}{P/\varepsilon-1+C_1}\frac{k}{\varepsilon}(P_{ij}-\tfrac{2}{3}P\delta_{ij})+\frac{1}{P/\varepsilon-1+C_1}\frac{k}{\varepsilon}A_{ij} \tag{12}$$

with the added convection terms as follows:

$$A_{ij}=\begin{vmatrix} 0 & \overline{uw}\dfrac{W}{r} & -\overline{uv}\dfrac{W}{r} \\ \overline{uw}\dfrac{W}{r} & 2\overline{vw}\dfrac{W}{r} & -(\overline{vv}-\overline{ww})\dfrac{W}{r} \\ -\overline{uv}\dfrac{W}{r} & (\overline{vv}-\overline{ww})\dfrac{W}{r} & -2\overline{vw}\dfrac{W}{r} \end{vmatrix} \tag{13}$$

The ASM constants are equal in magnitude to those used in the RSM model: $C_\mu=0.09$, $C_{\varepsilon 1}=1.44$, $C_{\varepsilon 2}=1.92$, $\sigma_k=1.0$, $\sigma_\varepsilon=1.3$, $C_1=2.5$, and $C_2=0.55$.

Thus the algebraic stress model applied in this study consists of five algebraic equations for the stresses: $\overline{uv}$, $\overline{vw}$, $\overline{uw}$, $\overline{v^2}$, and $\overline{w^2}$. The momentum equations are accompanied by the transport equations for kinetic energy, k, and its dissipation rate, ε.

The k–ε eddy-viscosity model. In addition to the anisotropic second-order closures, we also tested the widely used k–ε model of turbulence. We calculated isotropic turbulent viscosity using the values of k and ε obtained from their transport equations. The model constants are: $C_\mu=0.09$, $C_{\varepsilon 1}=1.44$, $C_{\varepsilon 2}=1.92$, $\sigma_k=1.0$, and $\sigma_\varepsilon=1.3$.

Numerical solution

Discretization and numerical solution of the transport equations introduce numerical diffusion in a similar way, as physical diffusion occurs in the real flow. Therefore choice of the discretization method for the convective terms of the transport equations is very important. The effects of numerical diffusion, associated with the first-order hybrid method[22] caused great concern with respect to its applicability to multidimensional flow.[17,18] In this study we used quadratic upstream differencing (QUICK) for discretization of the convective terms.

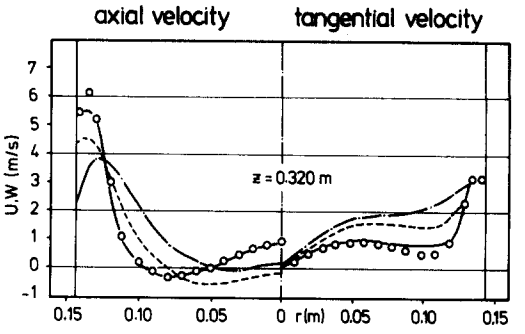

Figure 2 Importance of numerical scheme, flow case 3; measured and computed profiles of axial and tangential velocities 0.32 m downstream from vortex generator; ○ measurements; —— computed with QUICK and RSM; – – – computed with QUICK and k–ε; —·— computed with hybrid and k–ε

The importance of numerical solution is demonstrated in Figure 2. It shows measurements and predictions of flow case 3 for two numerical methods. The calculations utilized two models of turbulence: the RSM and the k–ε model. Figure 2 demonstrates that the differences in predictions obtained from first-order numerical solutions are comparable to the differences obtained from turbulence modeling, when the second-order numerical method is used. The QUICK method is not the only one that minimizes numerical diffusion; others are gradually becoming available.[23,24]

Numerical diffusion and numerical related errors should be reduced to the level that they become small compared to the physical diffusion of the flow considered. Thus for any numerical solution chosen, a fine enough numerical mesh has to be applied. As demonstrated by So *et al.*,[25] computations of low Reynolds number flows, where physical diffusion is small, required very fine grids of 78×66 nodes and a second-order numerical solution. However, the grid-independent predictions of high Reynolds number swirling flows reported in References 9 and 12 were obtained on meshes 40×35 and 48×48.

Table 2 provides information on the numerical grids used in our computations. Emphasis was placed on finding grid-independent solutions. For example, cases 9 and 11 were computed on coarse and fine grids. Figure 3 shows that increasing the mesh from 45×34 to 80×60 produces only marginal differences in predicted axial and tangential velocities. The burner quarl was represented in the computations by a series of steps. For short quarls ($B/A=1.5$), 8–10 steps usually were sufficient to represent the quarl shape properly, i.e., after that the flow was no longer dependent on the number of steps. For long quarls ($B/A=2$), at least 16 steps were required.

Table 2 Details of the computations (C = coarse grid; F = fine grid)

Case	Total number of grid nodes		Grid nodes in quarl		Applied model of turbulence		
	Axial	Radial	Axial	Radial	k–ε	ASM	RSM
3	59	27	16	8	×		×
9C	43	34	7	7	×	×	×
9F	60	40	9	9	×	×	×
11C	45	34	16	16	×	×	×
11F	80	60	24	24	×	×	×
40	45	34	16	16			×

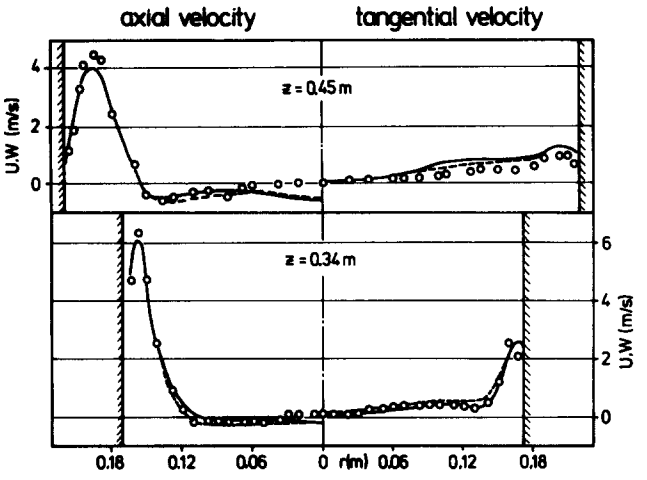

Figure 3 Effect of numerical grid on predicted flow patterns, flow case 11; ○ measurements; —— RSM predictions on grid 45 × 34; --- RSM predictions on grid 80 × 60

Inlet and boundary conditions

The computations require specification of initial conditions: values and profiles of both axial and tangential velocities, initial level of turbulence, k, and its rate of dissipation, ε. When we applied either ASM or RSM, we specified inlet values of the individual Reynolds stresses as $\frac{2}{3}k$ for normal stresses and calculated shear stresses using the k–ε effective viscosity and rate of strains. For all the flows considered, we took the measured values of axial and tangential velocities just upstream from the quarl as the inlet conditions. The computational inlet coincided with the first measurement traverse.

We estimated the inlet turbulence energy of the flows from the measured axial and tangential velocity fluctuations. We took the characteristic length scale of the turbulence—needed for estimation of the dissipation rate—to be $A/10$. Consequently, the inlet value of the dissipation of turbulence energy is

$$\varepsilon = \frac{C_\mu^{0.75} k^{3/2}}{0.007(A/2)} \tag{14}$$

We calculated velocities, turbulence energy, and the turbulence energy dissipation rate at the wall, using wall functions. At the wall, we set diffusion of all Reynolds stresses to zero. At the symmetry axis, we used a zero gradient condition for all variables.

Correct specification of outlet boundary conditions is of primary importance for successful prediction of highly swirling flows. Investigators have demonstrated experimentally[14,26] that, when a downstream flow is subcritical, an information about conditions at furnace exit propagates upstream and alters the flow. Hogg and Leschziner[12] examined the importance of formulation of downstream condition for computing swirling flows. They concluded that outlet conditions $\partial/\partial x = 0$ were appropriate only for supercritical downstream flows. We made our swirling-flow computations for a 4 m long cylindrical furnace. In flows 3, 11, and 40, there was no furnace exit contraction. In the computations, zero-gradient outlet boundary conditions were applied 4 m downstream, where no fluid was reentering the flow domain through the exit plane and the flow was experimentally identified as supercritical. In flow case 9, a 0.44-m diameter contraction was positioned at the furnace outlet. Therefore in the computations the furnace contained a contraction of the identical size. The computations were extended 0.3 m downstream from the contraction, where zero-gradient conditions were applied to the outlet's supercritical flow.

Anisotropy of turbulence

In the following sections, we frequently refer to *anisotropy of turbulence*. Its precise determination requires knowledge of all components of the Reynolds stress tensor. This knowledge can be gained if all six Reynolds stresses are measured, which requires difficult and elaborate experiments. The turbulence experimental data we utilize include only axial and tangential velocity fluctuations. Therefore a rough description of anisotropy of turbulence is given by fluxes of turbulence integrated over an entire cross section:

$$E(u_i) = 2\pi\rho \int_0^R \frac{\overline{u_i^2}}{2} U r \, dr \tag{15}$$

The fluxes show anisotropy between normal Reynolds stresses rather than give information about anisotropy of the entire stress tensor. In all our measured flows, we held constant the superficial axial velocity ($U_0 = 4.8\ \mathrm{m\,s^{-1}}$), so the quantity defined by Equation 15 can be used to compare flow anisotropy of different cases.

Swirling flows expanding into high confinement

If the ratio of furnace to inlet pipe diameter (D_f/A) is smaller than 3, we regarded the flows as highly confined. Otherwise, we considered them to be low-confinement flows.

Physics of the flows

Flow case 11 is a good example of highly confined swirling flows and therefore is analyzed here in detail. The flow geometry can be characterized by the confinement ratio (D_f/A) of 2.3 and the quarl expansion ratio (B/A) of 2. There was no end contraction on the experimental furnace. The ratio of furnace to quarl outlet diameter is 1.15, and therefore no external recirculation zone formed. The inlet vortex of low turbulence (1%) has a solid-body rotation and its swirl number is 0.75.

Figure 4 shows the measured flow pattern and mean flow characteristics. Consideration of the pressure distribution in swirling flows leads to a classical explanation of reverse-flow formation. In the straight-pipe inlet duct, the radial pressure distribution is such that the lowest pressure is always on the centerline. The pressure increases monotonically with radius ($dp/dr > 0$) in such a way that it balances the term $\rho W^2/r$. When the vortex leaves the straight pipe, it expands radially and both axial and tangential velocities decrease. The decrease in velocities generates an increase of the static pressure near the symmetry axis. Thus in a highly swirling flow, an adverse pressure gradient ($dp/dx > 0$) is created near the symmetry axis, and the flow direction reverses. This action implies that formation of the reverse flow is basically an inviscid phenomenon.

It is informative to consider Batchelor's simplified equation, which governs solid-body-rotation flows:[27]

$$\frac{\partial^2 \Psi}{\partial x^2} + \frac{\partial^2 \Psi}{\partial r^2} - \frac{1}{r}\frac{\partial \Psi}{\partial r} = r^2 \frac{dH}{d\Psi} - C\frac{dC}{d\Psi} \tag{16}$$

where H is the Bernoulli function,

$$H(\Psi) = \tfrac{1}{2}(U^2 + V^2 + W^2) + \frac{P}{\rho}$$

and C is the circulation

$$C(\Psi) = Wr$$

Equation 16 is valid for quasicylindrical, inviscid flows. It can provide information about the position of the zero streamline

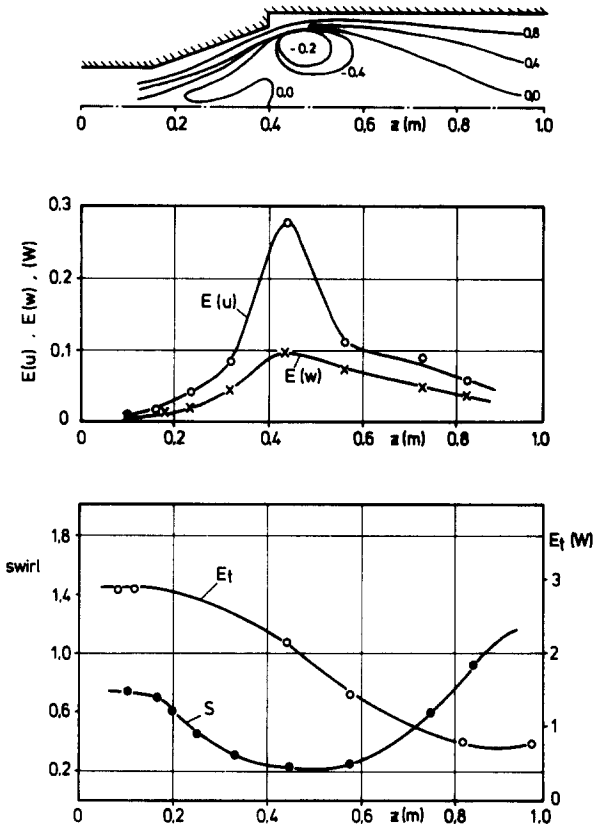

Figure 4 Flow case 11: measured flow pattern and main flow characteristics

inside the quarl and the numerical values of the axial and tangential velocities in the region located between the zero streamline and the quarl wall. Applying Equation 16 to flow case 11 results in a prediction that the first stagnation point is about 5 cm downstream from the quarl inlet. Equation 16 also predicts that, at the outlet of the quarl, the zero streamline is displaced from the symmetry axis by a radial distance of $0.85B$. (The measured displacement was $0.81B$.) Thus, using this simple inviscid flow equation, we can calculate the zero-streamline location in the quarl with good agreement with the measurements.

In fluid dynamics literature, another theory of swirling flows has been formulated over the last two decades or so. The theory is based on the concept of flow criticality, and it regards formation of the internal recirculation zone as a manifestation of a transition from a low swirl-number flow (called supercritical) to a high swirl-number flow (called subcritical). These two types of swirling flows have distinct properties; e.g., for supercritical flow, information about a downstream disturbance (contraction, probe, etc.) cannot propagate upstream in the flow, whereas in subcritical flow it can.[14,26] The determination of flow criticality involves solving Benjamin's equation.[28] For solid-body rotation, the solution indicated that the flow is supercritical if the ratio $W_{max}/(2U)$ is less than 0.96. The ratio $W_{max}/(2U)$ is simply the swirl number defined by Equation 3. For other type of vortices, the critical swirl number is not only a function of the tangential to axial velocity ratio but also the velocity distributions. Although the value of the critical swirl number can be estimated for quite a number of vortices,[14] Benjamin's critical equation has no general solution.

Figure 4 shows how flow criticality varies when the swirling vortex of case 11 expands. The swirl number calculated from the measured axial and tangential velocities is plotted as a function of distance from the vortex generator. The importance of rotational motion with respect to axial motion varies in the flow. The initial supercritical vortex ($S_0=0.75$) becomes even more supercritical upstream from the stagnation point. The downstream flow is highly subcritical, as indicated by the high values of the swirl number in this region.

The transition from a supercritical upstream flow to a subcritical downstream vortex is associated with a loss of total flow energy and generation of turbulence, as shown in Figure 4. The total flow energy is calculated from the measured values of time mean velocities and turbulence:

$$E_t=2\pi\rho\int_0^r\left(\frac{p-p_0}{\rho}+\frac{U^2+V^2+W^2}{2}\right)Ur\,dr$$

$$+2\pi\rho\int_0^r\left(\frac{\overline{u^2}+\overline{v^2}+\overline{w^2}}{2}\right)Ur\,dr \qquad (17)$$

The static pressure required for estimating total flow energy was obtained from the measured wall pressure by integrating the term $\rho W^2/r$. This pressure is valid strictly in the region where the flow is cylindrical, e.g., in the inlet duct and far downstream in the furnace. In the quarl and in the furnace where the recirculation bubble is formed, the estimate of total flow energy certainly is inaccurate. However, the overall energy loss is calculated correctly, because it involves the two cylindrical flows only. As shown in Figure 4, the energy of the inlet flow is 2.8 W while the downstream flow energy is only 0.8 W.

Figure 4 also shows the turbulence generated in the flow, with the axial component being larger than the tangential. Turbulence generation is maximum just downstream from the quarl in the region where strong reverse flow forms. Our measurements show that most of the turbulence is generated near the zero streamline, where high-velocity gradients occur. Little turbulence was generated at the walls, it dissipated rapidly, and the downstream flow was of low turbulence.

The comprehensive computer models should be able to predict (a) the inviscid part of the flows; (b) the generation and rapid decay of turbulence; and (c) the axial and tangential velocities in the downstream subcritical flow.

The computations

The predicted flow patterns are shown in Figure 5, and the time mean velocities are compared in Figure 6. The flow patterns predicted by RSM and ASM are similar and agree closely with the measured flow. The first stagnation point is correctly predicted by all three models. However, at the quarl outlet, the k–ε model predicts the radial displacement of the zero streamline to be $0.68B$, but the displacement of $0.8B$ was measured and predicted by the second-order closures. Thus the contribution of the viscous turbulent terms to the overall momentum balance in the quarl is overestimated in the k–ε formulation. Thus the rate with which the vortex loses its energy is too high, and, consequently, the position of maximum reverse flow ("eye" of the IRZ) is predicted inside the quarl instead of in the furnace. In the reverse flow region, the numerical values of the axial velocities predicted by the RSM and ASM are still far from perfect. The calculated maximum reverse flow was 28%, 26%, and 16% for the RSM, ASM, and k–ε model, respectively, whereas 44% was measured. Both second-order closures captured nicely the anisotropy of generated turbulence and the position of its generation, as shown in Figure 7. The k–ε model predicts generation of a high level of turbulence energy in the quarl, as shown in Figure 7(a). The ASM-computed values of normal Reynolds stresses agreed very closely with the RSM predictions.

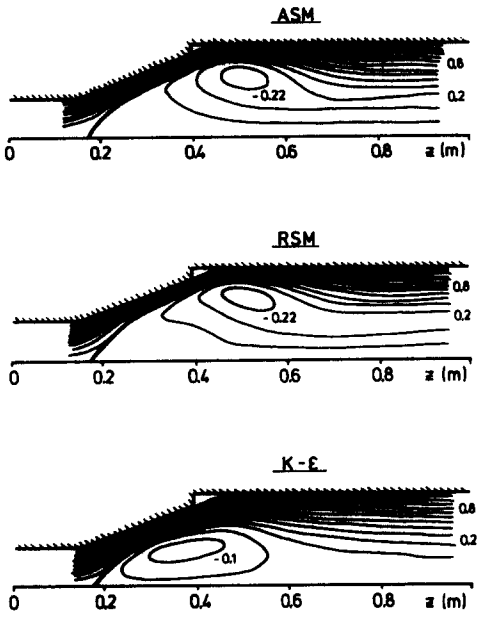

Figure 5 Flow case 11: predicted flow patterns; position of the zero streamline in the quarl plotted as thick line

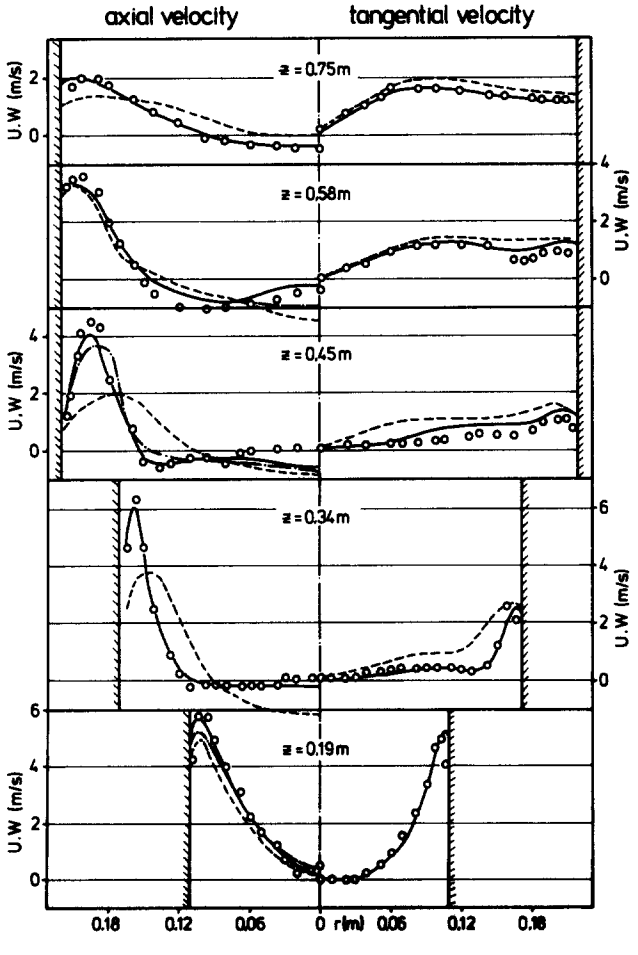

Figure 6 Flow case 11: measured and computed mean axial and tangential velocities; ○ measurements; —— RSM computed; —·— ASM computed; --- k–ε computed

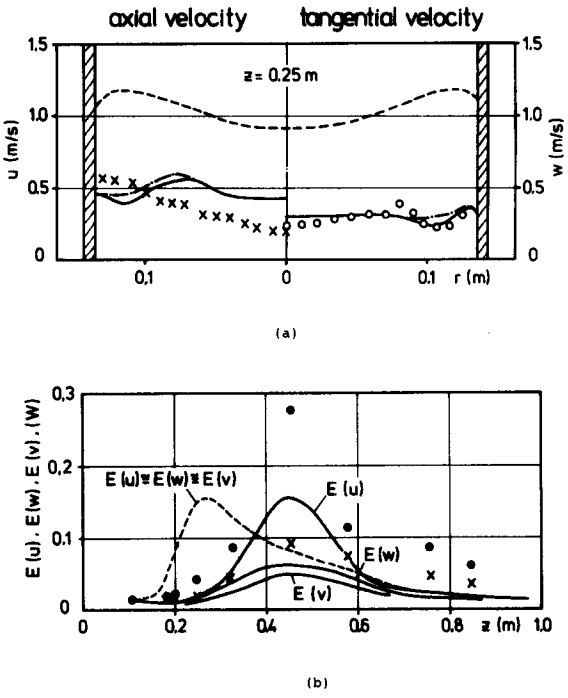

Figure 7 Flow case 11: properties of turbulence. (a) fluctuating velocities; ×, ○ measurements; —— RSM computed; —·— ASM computed; --- k–ε computed. (b) anisotropy in normal Reynolds stresses; ● $E(u)$ measured; × $E(w)$ measured; —— RSM computed; --- k–ε computed

Figure 8(a) shows how the inlet's solid-body-rotation vortex is transformed into an almost constant tangential velocity flow. The RSM and ASM predictions were very similar, and therefore only the RSM results are plotted. A good way of examining how tangential momentum is distributed within individual stream tubes is by plotting normalized circulation against normalized stream function. Such a plot, shown in Figure 8(b), indicates that the distribution of the tangential momentum in the downstream flow is correctly predicted by the second-order closures. However, surplus of tangential momentum near the symmetry axis results in axial velocities that are too low (negative). The k–ε predictions suffered from substantial deficiency of the tangential momentum downstream from the recirculation region.

Flow case 40 differs from case 11 only by a higher level of inlet turbulence. A turbulence generating grid, which was positioned in the inlet pipe, increased the inlet turbulence intensity to 5%. The measurements indicated that this turbulence was rapidly dissipated and altered neither the mean flow nor its turbulence. Computational results of case 40 were also very close to those of case 11. In case 3, an even smaller furnace was used, and the flow confinement was 1.53. Preliminary calculations of case 3 with the RSM and the k–ε model were reported previously,[29] and these confirmed superiority of the second-order closure.

Swirling flows expanding into low confinements

Physics of the flows

Expanding swirling flows issuing into a relatively large furnace, where an external recirculation zone (ERZ) may be present, are considered in flow case 9. The measured flow pattern is shown in Figure 9(a) and consists of two internal and one

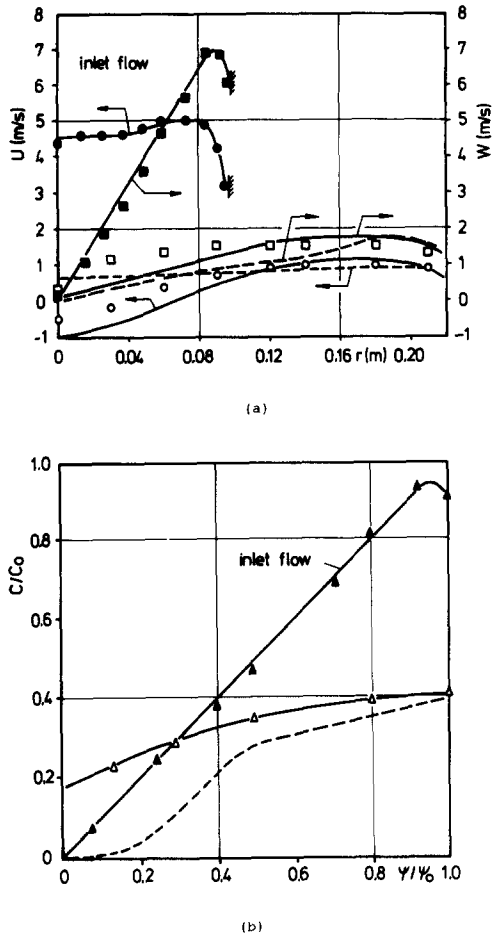

Figure 8 Flow case 11: properties of inlet supercritical vortex and subcritical flow at $z=1.2$ m downstream. (a) time mean velocities; ●, ■ measured velocities in the inlet flow (inlet conditions in the computations); ○, □ measured velocities in the downstream flow; —— RSM computed; --- k–ε computed. (b) normalized circulation versus normalized stream function; ▲ calculated from measured inlet velocities; △ calculated from measured downstream velocities; —— RSM computed; --- k–ε computed

external recirculation zones. The first IRZ originated in the burner quarl, and the second formed in the furnace. The radial displacement of the zero streamline at the outlet of the quarl measured $0.54B$, whereas $0.6B$ was obtained by solving Equation 16.

The width of an IRZ can be defined as the maximum radial displacement of the zero streamline that surrounds the region. Despite a lower confinement, the measured width of the first IRZ was $1.6A$ (flow case 9); $2A$ is applicable to flow case 11. Thus the strong external recirculation zone formed does not allow the swirling vortex to expand fully, and, consequently, the first IRZ is relatively weak; i.e., its measured reverse flow was only about 23%. However, as soon as the ERZ ends, the swirling flow expands further, forming a second reverse-flow region larger in physical size and having weaker velocities. Figure 9(b) shows both the anisotropic turbulence generated in the flow and its rapid dissipation.

The computations

The predicted flow patterns and velocities of flow case 9 are shown in Figures 10 and 11. Both the ASM and RSM predictions reproduce the two internal recirculation regions, but the k–ε calculations could not predict the existence of the second zone. The radial displacement of the zero streamline at the outlet of this short quarl was correctly predicted by the three models. The physical size of the external recirculation zone (ERZ) measured was reasonably well calculated when either the ASM or RSM was applied. The reverse flows in the ERZ were 106%, 92%, and 58% for the RSM, ASM, and the k–ε model predictions, respectively, compared to the 96% measured. The second-order closures captured nicely the flow features, and the time mean velocities were predicted accurately enough for engineering purposes (see Figure 11). The larger discrepancies appeared near the symmetry axis. Whether these

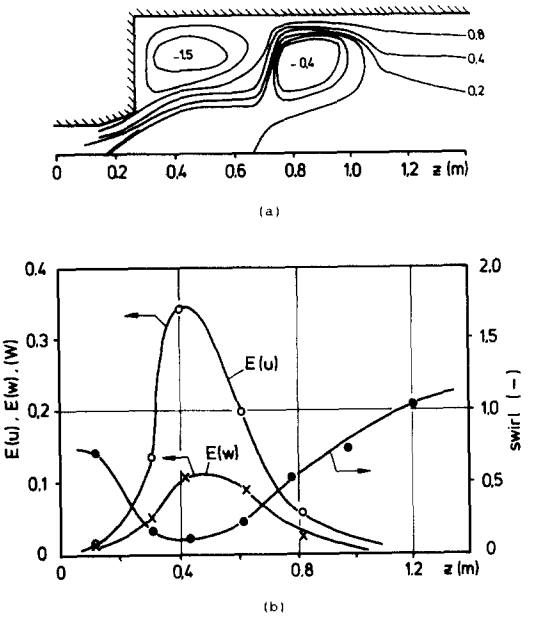

Figure 9 Flow case 9: (a) measured flow pattern; (b) main flow characteristics; position of zero streamline in the quarl plotted as thick line

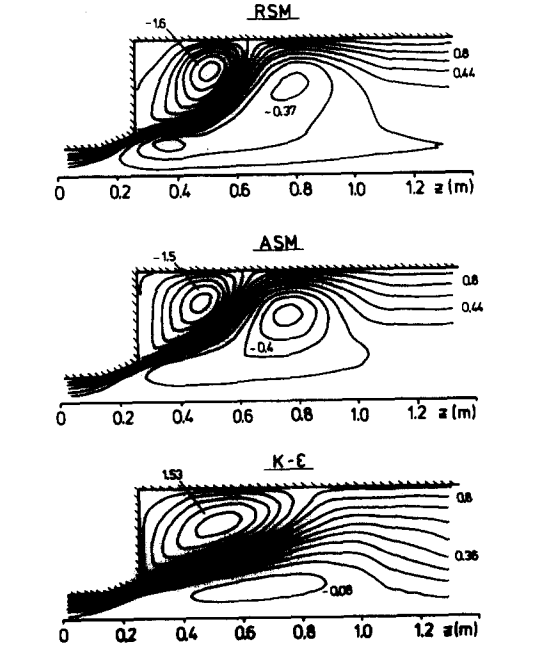

Figure 10 Flow case 9: predicted flow patterns

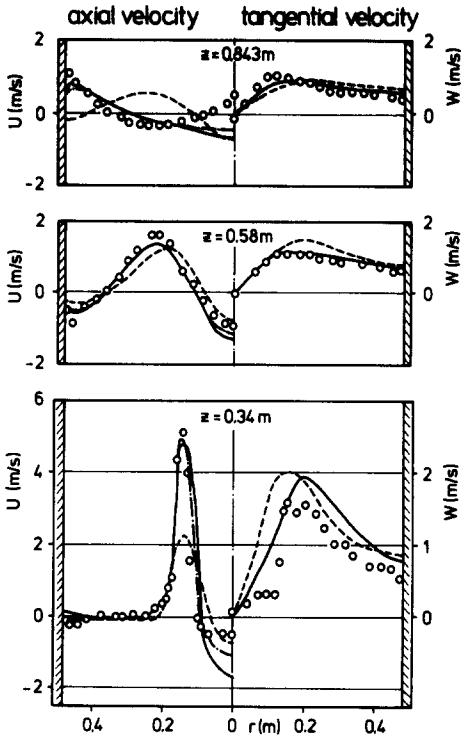

Figure 11 Flow case 9: mean axial and tangential velocities; ○ measurements; —— RSM computed; —·— ASM computed; – – – k–ε computed

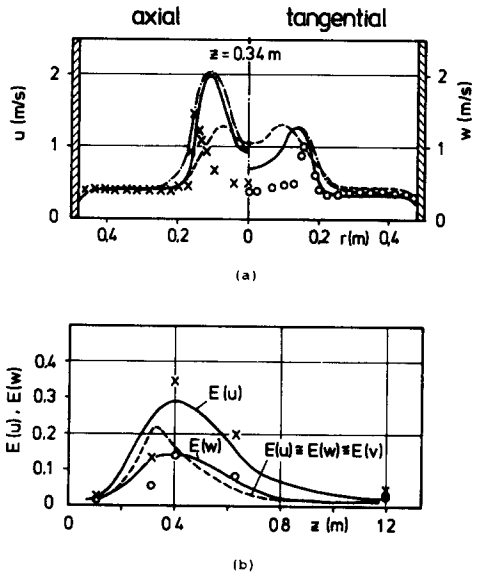

Figure 12 Flow case 9: properties of turbulence. (a) fluctuating velocities; × measured axial velocity; ○ measured tangential velocity; —— RSM computed; —·— ASM computed; – – – k–ε computed. (b) anisotropy in normal Reynolds stresses; × $E(u)$ measured; ○ $E(w)$ measured; —— RSM computed; – – – k–ε computed

discrepancies stem from the numerical scheme used, turbulence modeling, or perhaps the implementation of the zero-gradient boundary condition on the centerline is not clear.

The width of the first IRZ was calculated to be about 1.5B for the RSM and ASM predictions, which agreed perfectly with the measurements, but 1.25B was obtained from the k–ε model. The measured strength of the reverse flow was about 24%, compared to the 34%, 26%, and 4% predicted by the RSM, ASM, and k–ε model. The measured reverse flow in the second IRZ was 53%, whereas 47% and 75% were predicted by the RSM and ASM, respectively.

Axial and tangential fluctuating velocities were reasonably well predicted by the second-order closures, although at some stations—as illustrated in Figure 12(a)—the measured and computed values differed by a factor of 2. The measured anisotropy of turbulence was well represented in the predictions. The experimental evidence that most of the turbulence was generated on the boundaries of the first IRZ was also reflected in the computations. The very small differences between the RSM and ASM predictions indicate that transport of the Reynolds stresses played only a small role in the overall turbulence energy of the flow considered.

Figure 13 shows comparisons of measured and predicted properties of the downstream subcritical flow. With the exception of the centerline region, the second-order closures predicted reasonably well the time mean velocities and turbulence. Distribution of tangential momentum within individual stream tubes was well predicted by the RSM and ASM. In the k–ε predictions, about 50% of the downstream flow suffered from a deficiency of the tangential momentum, as shown in Figure 13(b).

Swirling flows with a central jet

Swirling annular flows with central, nonswirling jets are of considerable practical importance. Optimization of the interaction between these two streams may lead to a low-pollutant

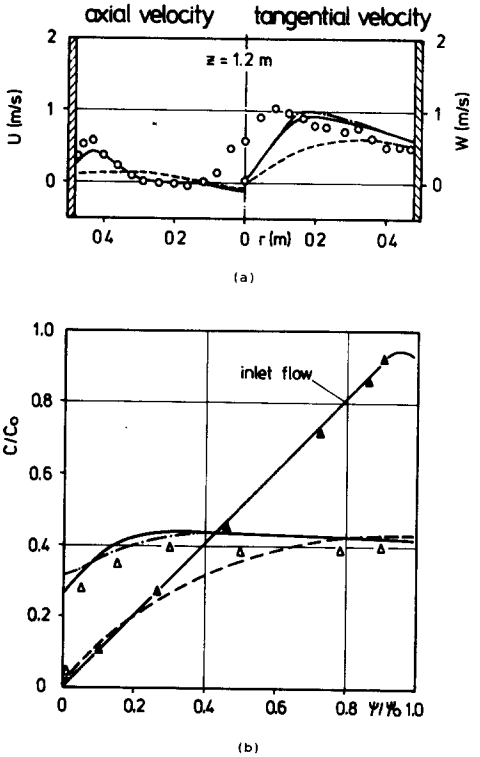

Figure 13 Flow case 9: properties of inlet supercritical vortex and subcritical flow at $z=1.2$ m downstream. (a) time mean velocities at $z=1.2$ m; ○ measurements; —— RSM computed; —·— ASM computed; – – – k–ε computed. (b) normalized circulation versus normalized stream function; ▲ calculated from the measured inlet velocities shown in Figure 8; △ calculated from the measured velocities at $z=1.2$ m; —— RSM predicted; —·— ASM predicted; – – – k–ε predicted

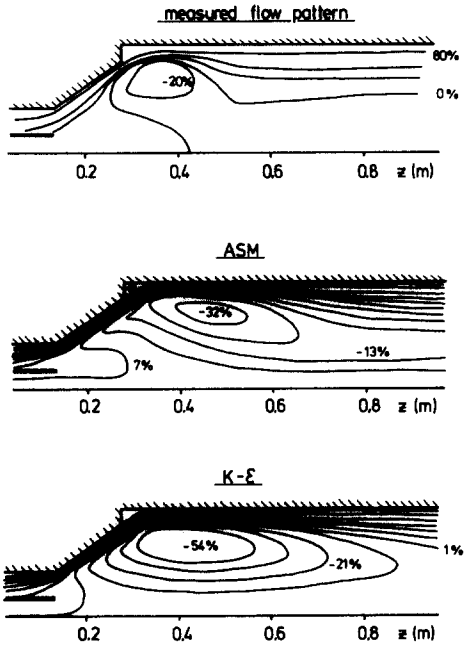

Figure 14 Measurements and predictions (60 × 32 grid) of swirling flow, with a central nonswirling jet; $S_0=1.5$, $B/A=2$, $\alpha=35°$, $D_t/A=2.3$, and $U_p/U_a=0.5$

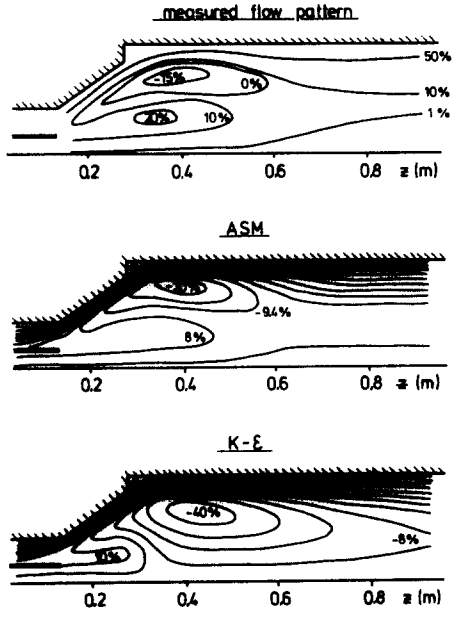

Figure 15 Measurements and predictions (60 × 32 grid) of swirling flow, with a central nonswirling jet; $S_0=1.5$, $B/A=2$, $\alpha=35°$, $D_t/A=2.3$, and $U_p/U_a=1$

burner design. Of special importance is optimization of the penetration depth of the central jet into the reverse flow.[6,7]

The mass flow rates of the central jet were 8% and 16% of the total flow. The mass mean velocities of the central jet were $2\,m\,s^{-1}$ and $4\,m\,s^{-1}$, respectively. The measurements, shown in Figures 14 and 15, indicate that the jet penetrated only partially into the reverse-flow region when the mass flow (and momentum) of the jet was low. However, when the flow rate was doubled, the jet penetrated the reverse flow almost completely.

The predicted flow patterns also are shown in Figures 14 and 15. Note that only in the ASM predictions is the jet penetration depth properly predicted. In the k–ε predictions the central jet is rapidly entrained in the surrounding swirling flow. Detailed comparison of the measurements and predictions reveals that, indeed, the rate with which the tangential momentum is transferred from the surrounding swirling flow to the nonswirling jet is substantially overpredicted by the k–ε model. Thus the outer layer of the jet picked up tangential momentum and deviated from the centerline. Without measurements of the shear stresses in the flow region where the central jet interacts with the reverse flow, however, we cannot conclude that the incorrectly predicted rate of tangential momentum transfer is the only reason for the k–ε model failure.

Conclusions

Measurements and predictions of a number of isothermal expanding swirling flows were reported. Three of the flows considered were highly confined flows, one was a low-confinement flow, and in two flow cases a nonswirling central jet was present. The flows were originally in solid-body rotation and expanded first into a burner quarl and then into a cylindrical furnace. The inlet flows had negligible radial velocity at the vortex generator, and their initial turbulence was not higher than 5% (see Equation 1).

We conclude that reliable engineering predictions of the swirling flows can be made if fine numerical grids are used in conjunction with the numerical QUICK method and either the RSM or the ASM is applied.

We identified three important regions in the solid-body-rotation flows considered: an initial region of almost inviscid expansion; a region of transition from a supercritical to a subcritical flow, where a substantially anisotropic turbulence was generated; and a subcritical downstream flow of low turbulence. The RSM and ASM predictions captured the overall flow behavior in all three regions. The k–ε computations began to fail in the burner quarl, where flow expansion was inviscid. The k–ε turbulent viscosities were about 30 times larger than the RSM (ASM) values in this region. This condition led to overprediction of the turbulent (viscous) terms in the Navier–Stokes equation. Neither the (anisotropic) generation of turbulence nor the distribution of the tangential momentum in downstream flow were correctly predicted by the k–ε effective-viscosity model. No substantial differences between the RSM and ASM predictions were observed. In the solid-body-rotation flows analyzed, transport of the Reynolds stresses was of no importance.

Computations of the two swirling flows with a central nonswirling jet were carried out with the ASM and the k–ε model. The rate with which the tangential momentum was transferred from the surrounding swirling flow to the nonswirling jet was substantially overpredicted by the k–ε model. Consequently, the jet deviated rapidly from the symmetry axis and did not completely penetrate the reverse flow as it was measured. The ASM-predicted flow patterns agreed well with those measured. The ASM-computed rate of the tangential momentum transfer to the jet was substantially lower than that of the k–ε model. Measurements of the shear stresses in the flow region where the central jet interacts with the reverse flow are needed in order to confirm this reasoning.

Acknowledgments

We thank the Joint Committee of the International Flame Research Foundation for permission to publish this article.

It contains experimental results obtained within the IFRF member-funded project Near Field Aerodynamics (NFA) of Swirl Burners. The contributions of S. Bortz, J. Dugué, A. Hagiwara, H. Horsman, and C. Schmid to the NFA programme are greatly appreciated. We also gratefully acknowledge the financial support of the IEA Coal Combustion Science Programme, Annex 2, sponsored by organizations in Canada, the Federal Republic of Germany, and The Netherlands. The computations were carried out with the computer code "Fluent."

References

1 Beer, J. M. and Chigier, N. Stability and combustion intensity of pulverized coal flames—effect of swirl and impingement. *J. Inst. Fuel.*, 1969, **42**, 433

2 Leuckel, W. and Fricker, N. The characteristics of swirl-stabilised natural gas flames. Part 1: Different flame types and their relation to flow and mixing patterns. *J. Inst. Fuel*, 1976, **49**, 103

3 Gupta, A. K., Lilley, D. G., and Syred, N. Swirl Flows, Abacus Press, 1984

4 Hillemans, R., Lenze, B. and Leuckel, W. Flame stabilization and turbulent exchange in strongly swirling natural gas flames. *Proc. Twenty-First Symp. (Int.) on Combustion*, Munich, 1986, 1445

5 Truelove, J. S. Prediction of the near–burner field and combustion in swirling pulverised–coal flames. *Proc. Twenty-First Symp. (Int.) on Combustion*, Munich, 1986, 275

6 Weber, R., Smart, J. P., and Phelan, W. NOx reduction with coal firing by application of both internal air staging and fuel rich precombustors. Report on the AP 14 trials. IFRF Doc. No. F 037/a/16, 1987

7 Smart, J. P. and Weber, R. NOx reduction and burnout optimisation using aerodynamically air staged burner and an air staged precombustor burner. *J. Inst. of Energy*, 1989, **62**, 237

8 Launder, B. E. Turbulence modelling of three-dimensional shear flows. Paper presented at AGARD 63rd FDP Symp. on Fluid Dynamics of 3D Turbulent Shear Flows and Transition, Cesme, Turkey, Oct. 3–6, 1988

9 Fu, S., Huang, P. G., Launder, B. E., and Leschziner, M. A. A comparison of algebraic and differential second-moment closures for axisymmetric turbulent shear flows with and without swirl. *J. Fluids Eng.*, 1988, **110**, 216

10 Sislian, J. P. and Cusworth, R. A. Laser Doppler velocimetry measurements in a free isothermal swirling jet. University of Toronto Institute of Applied Science Report No. 281, CN ISSN, 0082-5255, 1984

11 Ribeiro, M. M. and Whitelaw, J. H. Coaxial jets with and without swirl. *JFM*, 1980, **96**, 769

12 Hogg, S. I. and Leschziner, M. A. Computations of highly swirling confined flow with a Reynolds stress turbulence model. *AIAA J.*, 1989, **27**(1), 57

13 So, R. M., Ahmed, S. A., and Mongia, H. C. An experimental investigation of gas jets in confined swirling air flows. NASA CR-3832, 1984

14 Hagiwara, A., Bortz, S., and Weber, R. Theoretical and experimental studies on isothermal, expanding swirling flows with application to swirl burner design. Results of the NFA 2-1 investigations. IFRF Doc. No. F 259/a/3, 1986

15 Schmid, C., Bortz, S., and Weber, R. Further experimental studies on isothermal expanding swirling flows with application to swirl burner design. Results of the NFA 2-2 investigation. IFRF Doc. No. F 259/a/4, 1987

16 Launder, B. E. and Morse, A. Numerical predictions of axisymmetric free shear flows with a second order Reynolds stress closure. *Turb. Shear Flows I*, Springer-Verlag, Heidelberg, 1978, 279

17 Leschziner, M. A. and Rodi, W. Calculation of annular and twin parallel jets using various discretization schemes and turbulence model variations. *Fluids Eng.*, 1981, **103**, 352

18 Sturgess, G. J. and Syed, S. A. AIAA paper No. 85-0060, 1985

19 Launder, B. E. and Spalding, D. B. The numerical computation of turbulent flows. *Computer Meth. in Appl. Mech. and Eng.*, 1974, **3**, 269

20 Rodi, W. *ZAMM*, 1976, **56**, 213

21 Sloan, D. G., Smith, P. J., and Smooth, L. D. Modeling of swirl in turbulent flow systems. *Prog. in Energy and Comb. Sci.*, 1986, **12**, 163

22 Spalding, D. B. A novel finite–difference formulation for differential expressions involving both first and second derivatives. *Int. J. Num. Meths. Eng.*, 1972, **4**, 551

23 Raithby, G. D. A critical evaluation of upstream differencing applied to problems involving fluid flow. *Computer Meth. in Appl. Mech. and Eng.*, 1976, **9**, 75

24 Shyy, W. and Correa, M. AIAA paper No. 85-0400, 1985

25 So, R. M. C., Lai, Y. G., Hwang, B. C., and Yoo, G. J. Low-Reynolds-number modelling of flows over a backward-facing step. *J. Appl. Math. and Physics*, 1988, **39**, 13

26 Escudier, M. P. and Keller, J. J. Recirculation in swirling flow: A manifestation of vortex breakdown. *AIAA J.*, 1985, **23**, 111–116

27 Batchelor, G. K. *Introduction to Fluid Dynamics*, Cambridge University Press, 1985

28 Benjamin, T. B. Theory of the vortex breakdown phenomenon. *J. Fluid Mech.*, 1962, **14**, 593–628

29 Weber, R., Boysan, F., Swithenbank, J., and Roberts, P. A. Computations of near field aerodynamics of swirling expanding flows. *Proc. 21st Symp. (Int.) on Combustion*, Munich, 1986, 1435–1443